Published in final edited form as:
Anal Chem. 2010 May 15; 82(10): 4063–4071. doi:10.1021/ac902975r.

Development of a Photothermal Absorbance Detector for Use with Microfluidic Devices

Patty J. Dennis[†], **Erin R. Ferguson Welch**[†], **Jean Pierre Alarie**[†], **J. Michael Ramsey**[†,*], and **James W. Jorgenson**[‡,*]

[†] Department of Chemistry, University of North Carolina at Chapel Hill, Chapman Hall Room 251, Chapel Hill, North Carolina 27599-3216

[‡] Department of Chemistry, University of North Carolina at Chapel Hill, Kenan Laboratories Room A308, Chapel Hill, North Carolina, 27599-3290

Abstract

The development of a photothermal absorbance detector for use with microfluidic devices is described. Unlike thermooptical techniques that rely on measuring refractive index changes, the solution viscosity is probed by continuously monitoring solution conductivity. Platinum electrodes microfabricated on a quartz substrate and bonded to a substrate containing the microchannels enable contact conductivity measurements. The effects of excitation frequency and voltage, electrode spacing, laser power, and laser modulation (chopping) frequency were evaluated experimentally. In the current configuration a limit of detection of 5 nM for DABSYL-tagged glucosamine was obtained using long injections (to give flat-topped peaks). This corresponds to an absorbance of 4.4×10^{-7} AU. Separation and detection of DABSYL-tagged glycine, proline, and tryptophan is also shown to demonstrate the feasibility of the method. In addition, simulations were used to investigate the applicability of the technique to small volume platforms.

Introduction

One of the challenges facing microcolumn separation techniques, including capillary and microfabricated fluidics-based (microchip) separations, is the need for a universal, highly sensitive method of detection. Fluorescence and electrochemical detection are frequently employed in microchip chromatographic or electrophoretic techniques because of their inherent low-mass sensitivity. These detection methods, however, have limited applicability. Only those analytes that are intrinsically electroactive, natively fluorescent, or are amenable to labeling with appropriate tags, may be detected. UV absorbance detection is less selective and one of the most commonly used optical detection methods but the signal is path-length dependent and does not provide high sensitivity for on-line small dimension column analysis. Attempts to improve sensitivity by increasing the optical pathlength have included the development of the Z-cell,[1, 2] bubble-cell,[3] and U-cell,[4] but these have had limited success due to the increase in band broadening resulting from changes in geometry at the detection point.

Other approaches that appear promising for obtaining highly sensitive, broadly applicable detection with capillary columns rely on the measurement of photothermal effects.[5] These techniques rely on the physical changes in solution that occur when an analyte absorbs light as it passes through an optical excitation beam. The nonradiative relaxation of the analyte

[*]Corresponding Authors: [†]jmramsey@unc.edu. Fax: (919) 962-4952 and [‡]jj@unc.edu. Fax: (919)962-2388.

increases the temperature of the sample solvent resulting in changes in refractive index (RI) and viscosity. In aqueous solutions the RI changes 0.01 % per degree temperature change while the relative ΔRI in organic solvents is 0.04% per degree temperature change.[6] Although these values are detectable, a more sensitive measure is solution viscosity since it changes ~2% per degree temperature change for organic or aqueous solutions, a change that is 50–200 times greater than RI.[6]

Detecting viscosity changes in capillary columns and on microfluidic platforms is a difficult task to accomplish. Solution viscosity, however, can be directly related to electrical conductivity, an easily measurable parameter, through a variation of the Stokes-Einstein equation:

$$\mu = \frac{ez}{6\pi\eta r} \tag{1}$$

where μ is the ion mobility, e is the fundamental charge on an electron, z is the ion charge, η is the solution viscosity, and r is the solvated ion radius. From this equation, the viscosity can then be related to electrical conductivity using the following:

$$\kappa = F\sum_i z_i \mu_i c_i \tag{2}$$

where κ is the electrical conductivity, F is Faraday's constant, and c_i is the concentration of each species in solution. Combining equations 1 and 2 results in equation 3, showing the relationship between viscosity and electrical conductivity.

$$\kappa = \frac{eF}{6\pi\eta}\sum_i \frac{z_i^2 c_i}{r_i} \tag{3}$$

Contact conductivity detection has previously been investigated in capillary systems.[7–10] This method was first applied to on-column capillary electrophoresis (CE) analysis by Huang et. al. [7] Platinum wire electrodes, 25-μm in diameter, were placed directly opposite each other through 40-μm diameter holes drilled into the walls of fused silica capillaries. Lithium in human serum was quantified and low molecular weight carboxylic acids were detected using this approach.[8–10] Construction of the detector, however, made this technique difficult to implement and as a result, it has not been widely used.

In 1998, two research groups independently developed a contactless conductivity detector for use with CE.[11–12] Da Silva and do Lago developed a detection cell by painting two 2-mm wide silver electrodes separated by a 1-mm gap onto the outside of a fused silica capillary.[11] They separated inorganic cations and achieved a limit of detection of 1.5 μM for the lithium ion. Zemann and co-workers used 15–50-mm long electrodes made from syringe cannulae for their electrodes.[12] Inorganic cations and anions were determined and limits of detection on the order of 200 ppb (≈ 10 μM) were obtained for sodium and chloride.

It was not until 2001 that conductivity detection was applied to microfluidic chips.[13–14] Laugere *et al.* introduced a capacitively coupled 2- and 4-electrode conductivity detector for the detection of simple ions.[13] Guilt *et al.* introduced a contact conductivity detector for use with microfluidics in the same year.[14] For this setup, detection limits of 5 μM were obtained

for tartaric and fumaric acids.[15] Since its implementation on microfluidic platforms there have been numerous reports characterizing this detector[16–22] and describing applications.[23–29]

Our laboratory has previously investigated the photothermal effect in 50-μm (diameter) capillary columns.[30] A capacitively coupled, contactless conductivity detector was used to measure photothermal effects of 48-μM DABSYL-glucosamine (29,600 M^{-1} cm^{-1}) in 20-mM Borate buffer and it was experimentally determined that a 200-mW, 488-nm light source modulated at 4 Hz would cause an approximate 1-mV signal. This value represents only a 0.26% change over the 380 mV background signal that was observed. Calculations, however, indicate that an 11% change (40 mV on a 380 mV background) would be expected for detection in a 50-μm id capillary using a 1-mm electrode gap. This discrepancy between the experimentally determined and anticipated values led to the development of a theoretical model for the detection system. The simulations indicate that the capacitive nature of contactless conductivity detection gives rise to a sensing region that is much larger than the volume that is thermooptically heated, decreasing signal intensity and overall sensitivity. The sensing region for contacting electrodes, on the other hand, is restricted to the volume of fluid between the electrodes, which should bring detection sensitivity in closer alignment with theoretical values. Although a detection scheme that relies on this type of electrode configuration is difficult to implement on a capillary system, contacting electrodes may be easily fabricated on a microfluidic platform. In this work the development of a photothermal absorbance detector that is based on contact conductivity measurements on a microfluidic device is presented. The electronics for the detector are similar to those used with the capillary conductivity photothermal system previously developed in the Jorgenson research lab.[30]

Experimental

Materials and Buffers

All materials were used as received without further modification. Rhodamine B, 2-morpholinoethansulfonic acid (MES), and L-histidine and were purchased from Sigma (St. Louis, MO). Sodium hydroxide solution (NaOH) was obtained from Fisher Scientific (Fair Lawn, NJ) and 2′,7′–dichlorofluorescein (laser grade) was obtained from Acros Organics (Geel, Belgium). Glucosamine and 4-dimethylaminoazobenzene-4′-sulfonyl (DABSYL) chloride were obtained from Supelco (St. Louis, MO) and DABSYL-tagged glycine, proline, and tryptophan were purchased from Anaspec (San Jose, CA). All buffer and sample solutions were prepared using deionized water (Barnstead Nanopure Filtration System, Boston, MA) and were filtered prior to use with 0.2-μm nylon membrane filters from Whatman (Brentford, Middlesex, UK). The electrophoresis run solution was 20 mM MES/20 mM histidine at pH 6.1.

Preparation of DABSYL-tagged glucosamine (DABSYL-Glu)

Tagging of Glu with DABSYL has been described in detail elsewhere.[30–33] Briefly, equal volumes of a 6-mM solution of DABSYL chloride in acetone and a 1-mM solution of Glu in 50 mM potassium carbonate buffer (pH 9.0) were mixed and heated in a water bath at 75°C for 12 min. The mixture was then cooled to room temperature, frozen by immersion in liquid nitrogen, and placed in a vacuum oven to remove solvent. The lyophilized powder was suspended in 10 mL deionized water and the suspension sonicated for 10 min and then centrifuged at 15,000 rpm for 15 min. The liquid was decanted and the procedure repeated 4–5 times. Deionized water was added to the final pellet and the sample frozen until use. All experimental studies were performed with 50 μM DABSYL-Glu.

Optical System

A schematic diagram of the setup used for photothermal detection is shown in Figure 1. The light source was an adjustable power Innova 300 FReD laser operated at 488 nm (Coherent, Santa Clara, CA) and modulated at 20 Hz (unless otherwise stated) using an SR540 optical chopper (Stanford Research Systems, Sunnyvale, CA). The beam was spatially filtered using a 25-μm pinhole (Melles Griot, Albuquerque, NM) to remove any stray light. A long working distance 40× microscope objective (Olympus, Center Valley, PA) was used to focus the beam to give a sub-10-μm spot size within the microfluidic channel. An F/2 fused silica singlet lens was used to focus the image before passing the beam through two neutral density filters (FNQ057 and FNQ065, Melles Griot, Irvine, CA) and being viewed with a PL-A741 machine vision camera (PixeLINK, Ottawa, ON).

Electronic Components

Two DS345 digital function generators (Stanford Research Systems, Sunnyvale, CA) were used to supply the AC excitation signal to the conductivity cell. All measurements were taken under zero background conditions by adjusting the phase and voltage of the function generators to null the background conductivity, using a master-slave configuration. The frequency used for all studies, with the exception of frequency dependent investigations, was 100 kHz, based on the frequency input limit of the lock-in amplifier. 1–10 V excitation signals were connected to the electrodes through 3-kV, 100-pF radial disc capacitors (Panasonic-ECG, Secaucus, NJ). A 316 stainless steel compression spring (Small Parts Inc., Miami Lakes, FL) equipped with an aluminum pad soldered to the end was used for connection to the electrode pad. The detection electrode was connected to the amplifier through a 3-kV, 100-pF radial disc capacitor to prevent any direct current (DC) voltage from reaching the detection electronics.

An OPA602 operational amplifier (Texas Instruments, Dallas, TX) was used in a current- to-voltage configuration with a 1-MΩ feedback resistor (Multicomp, Chicago, IL) giving a gain of 10^6 V/A. Power was supplied to the operational amplifier using a Model 1301 Power Supply (Global Specialties, New Haven, CT) at ± 15 V. Capacitors (1 nF, Newark Electronics, Chicago, IL) were added in parallel with the power supply to remove any high frequency oscillations that were manifested in the feedback loop of the operational amplifier.

Two SR810 digital lock-in amplifiers (Stanford Research Systems, Sunnyvale, CA) were used for signal isolation and amplification in all cases. The external reference setting was used on both lock-in amplifiers. The first lock-in amplifier reference was supplied by a split signal from the master DS345 function generator. The second lock-in amplifier reference was supplied by the "f" output of the SR540 optical chopper and was based on the modulation (chopping) frequency of the laser light giving the photothermal reference. The first lock-in amplifier used a 1-ms time constant and a 24-dB/octave slope, giving a bandwidth of 78 Hz for all experiments except those involving variations in modulation frequency where the time constant was changed to provide the narrowest possible bandwidth. The output of the first lock-in amplifier was sent to the second (photothermal) lock-in amplifier. The second lock-in amplifier used a 100-ms time constant and a 24-dB/octave slope for all cases, giving a bandwidth of 0.78 Hz. While it was experimentally determined that the maximum background conductivity was obtained at an excitation frequency of 170 kHz (data not shown), signal measurements above 100 kHz necessitate the use of a high frequency input lock-in amplifier. An SR844 RF lock-in amplifier was used at 170 kHz; however, it was determined to give noise values that were nearly double those seen with a lower frequency lock-in amplifier (data not shown). It is thought that the increase in noise associated with the RF lock-in amplifier is a result of coherent pickup in the reference signal pathway. For this reason, all analyses were completed using the SR810 lock-in amplifier, limiting the excitation frequency to 102 kHz. The sensitivity of each lock-in amplifier was chosen so that the maximum signal could be obtained for a given range.

The output of both lock-in amplifiers was digitized using a USB-6229 DAQ card (National Instruments, Austin, TX) and collected on a personal computer using custom software written in LabVIEW (National Instruments, Austin, TX). Data analysis was performed in Igor Pro (Wavemetrics, Lake Oswego, OR) and included median filter baseline subtraction prior to analysis. Noise measurements were taken from the background conductivity measurement over the time frame approximately equal to the width of a peak.

Microchip Fabrication

Microchips were fabricated from quartz substrates (Telic, Valencia, CA) using standard photolithography and wet chemical etching techniques. Substrates containing the fluidic channels were bonded using a previously described procedure [34] to coverplates containing the excitation and detection electrodes. A simple cross chip design was used (see Figure 1) with a separation channel length of 3.5 cm. All channels were 70-μm wide and 30-μm deep. The electrodes (oriented perpendicular to the channel) were 50-μm wide and were spaced 25–100-μm apart. The interdigitated excitation and detection electrodes overlapped by 100-μm. The coverplate was patterned with the electrode geometry using a positive photoresist. The coverplate was wet etched 100-nm deep to create shallow trenches in which the metal electrodes where deposited to keep the surface as planar as possible for bonding purposes. An ion deposition system (South Bay Technologies, San Clemente, CA) was used to deposit 2–30 nm of chrome followed by 15–70 nm of platinum. Excess metal was removed in a lift-off [35] manner by submersing and sonicating the substrate in acetone, leaving the chrome/platinum layer in the desired electrode pattern. Vias were drilled into the cover plates prior to bonding to provide access to the channels and small glass cylinders were affixed using a UV curable optical adhesive (Norland, Cranbury, NJ) over these holes to serve as fluid reservoirs.

Electrophoresis System

Electrophoresis was performed using a laboratory built high voltage power supply with six high voltage output modules (10A12-P4 UltraVolt, Ronkonkoma, NY). Inputs to the high voltage power supplies were driven by the analog output of a USB-6229 DAQ board (National Instruments, Austin, TX) and controlled by a custom program written in LabVIEW (National Instruments, Austin, TX). High voltage outputs were applied to the chip reservoirs via platinum electrodes. Gated injections were performed electrokinetically by modifying the magnitude and duration of the voltages applied to the reservoirs on the microchip.[34] A TE300 inverted microscope (Nikon, Melville, NY) equipped with a 20X objective, a high pressure mercury lamp, and a CCD camera (Roper Scientific, Trenton, NJ) were used to visualize and optimize injection profiles of either fluorescein or rhodamine B in run buffer.

Photothermal Simulations

Dynamic simulations were used to investigate photothermal effects in a microchip channel and a capillary column. Simulations were performed using CoventorWare 2006 (Coventor, Inc., Cary, NC) software and inputs for channel geometry were based on those used experimentally. Quartz was specified as the substrate and platinum was used as the electrode material. All simulations were based on a 200-mW light source modulated at 20 Hz. The maximum average temperature was calculated for the region between the electrodes: 50-μm × 100-μm × 30-μm (total volume of 0.15 nL) for the microchip-based simulations and 1-mm × 50-μm × 50-μm (about 2 nL) for capillary-based simulations. Since the software precluded the analysis of heating and heat dissipation in combination with fluid flow, all simulations were based on static fluid elements. MemCFD solver was used to compute the average temperature due to heating. [36]

Results and Discussion

Photothermal Simulations

Simulations have been performed for a microfluidic system using input parameters similar to those used in the previous study but taking into account heat dissipation due to convection to provide greater accuracy. The schematic geometrical configuration of the model used is shown in Figure 2. This geometry was used for both capillary and microfluidic simulations with dimensions appropriate for each case as stated above. It was determined that a 12-mV change should be expected given a background conductivity of 380 mV for the capillary-based system. Due to the capacitive nature of the signal application and detection, the actual change in detection is expected to be lower than predicted and was confirmed experimentally. Simulations for the microfluidic device resulted in a theoretical temperature change of nearly 9°C, or a conductivity signal change of approximately 68 mV, given the same 380 mV background. Since the electrical signal is not capacitively coupled to the solution in this case, these values should more accurately reflect actual changes in conductivity. This simulation also serves to highlight the increased sensitivity that could be achieved with a microfluidic device using contact conductivity detection.

Additional simulations were performed to optimize the signal that could be obtained using a microfluidic device. The effects of the detection cell geometry (i.e., electrode spacing) and laser placement were examined. It was experimentally determined that the location of the laser spot has a substantial effect on the signal due to the absorption of light (and associated heating) by the electrodes. Electrode heating increases the temperature in the surrounding solution contributing to the background signal. Thus, it was important to investigate electrode spacing to maximize the signal intensity while minimizing the detrimental effects of electrode heating. For this simulation, a model based on a 20-μm deep channel and 20-μm diameter laser spot was used. The average solution temperature was used to determine the effect of electrode spacing by running a set of simulations with various detection gap sizes. Based on the spatial heat distribution using laser powers from 25 mW to 1 W it was determined that 100 μm from the laser spot center, the increase in temperature would be less than 1%, indicating that a detection gap of 200 μm would encompass 99% of the heated solution (Figure 3A). Thus, using a 200-μm detection gap with a laser spot placed near the center of the gap would ensure that any additional signal arising from electrode heating would be minimized. It is thought that narrower electrode spacings increase the likelihood that some of the incident laser light will strike the electrodes and be absorbed, creating heat that can be conducted into the solution, lowering the viscosity, and generating additional background signal. In a separate simulation, however, the importance of placing the electrodes as close together as possible was established. As shown in Figure 3B, the change in conductivity increases with smaller electrode spacings, demonstrating the importance of finding an electrode spacing that is narrow enough to give the maximum signal without generating additional erroneous signal from electrode heating. Additionally, it was also determined that higher signals could be obtained with smaller laser spot diameters due to confinement of solvent heating to a more central location and increased time for thermal conduction to the substrate.

The effect of laser power on the photothermal response was also investigated. Unlike other absorbance techniques, where the signal is proportional to the ratio of the incident power to the power transmitted though the sample, photothermal absorbance detection is directly proportional to the power absorbed, which is the determining factor in the sensitivity of the detection method. By defining the power absorbed (P_{ABS}) as the difference in the incident (P_O) and transmitted power, the following relationship can be obtained (equation 4)

$$P_{ABS}=P_O(1-10^{-\varepsilon bc}) \quad (4)$$

where ε is the molar absorptivity, b is the path length, and c is the concentration. This equation can be approximated using a Taylor series expansion and rearranged to show that the power absorbed is directly proportional to the absorbance (A) and the incident power (equation 5) since the light being absorbed is less than 5% of the incident light. Thus, by increasing the incident power, more light should be absorbed, providing for a more sensitive measurement.

$$P_{ABS}=2.303P_O\varepsilon bc=2.303P_OA \quad (5)$$

For these simulations, laser powers in the range of 5–500 mW were applied to a 10-μm deep microchip and an increase in signal intensity with increasing laser power was confirmed for a 50-μm × 50-μm thermooptically heated region. Simulations were also performed using deeper channels, and it was found that the power dependence holds true for all depths investigated (Figure 3C). We also investigated the signal dependence on path length, or correspondingly on channel depth. Simulations were performed using various channels depths while maintaining a channel aspect ratio of 0.25 to mimic experimentally used microchips that were fabricated using isotropic wet chemical etching. The fixed aspect ratio implies that channel width increases linearly with channel depth. These simulations indicate a nonlinear signal dependence on path length (channel depth) (Figure 3D) and suggest that there are two variables affecting the signal. As the channel depth decreases toward zero, the surface to volume ratio is increasing as the reciprocal of the depth leading to increased heat conduction to the substrate. With increasingly large channel depth, the volume of fluid within the detection zone increases as the channel depth squared but the deposited energy increases linearly. Therefore, the energy per unit volume decreases as the reciprocal of the channel depth, decreasing the overall average temperature. As shown in Figure 3D, there is an optimal channel depth that will depend on the substrate thermal conductivity and was found to be approximately 50 μm for this simulation.

Electronic Characterization

As discussed previously and shown above, the detector cell geometry has a large effect on the conductivity signal. This has been experimentally determined over the last several years with capillaries.[37–40] Our computer simulations for microfluidic devices indicate a similar dependence. To fully characterize this dependence the effects of excitation signal (frequency and voltage) and electrode spacing were experimentally investigated using our current microfluidic device (30-μm deep channels with 50-μm electrode spacing). For all characterization studies, a 7-second long gated injection is used to give a flat-topped peak. This allows for accurate quantification of the detector response, in addition to providing the ability to very clearly observe signal modulation. The effect of excitation frequency on the photothermal signal–to-noise ratio (S/N) using a three-electrode setup is shown in Figure 4. Data were obtained using an excitation voltage of 5 $V_{p\text{-}p}$ and 48-mW laser power (20-Hz modulation) with a 50-μM DABSYL-Glu sample. The signal was measured for excitation frequencies in the range of 5–100 kHz. The photothermal response was observed to increase with higher excitation frequencies. This is in agreement with previously published results for the response in a capillary system[30] and can be explained by considering a simple RC circuit. At low frequencies, more of the excitation voltage is dropped across the capacitor due to high impedance; however, at higher frequencies, the majority of the voltage is dropped across the detection cell, increasing the signal intensity.

The effect of excitation voltage on the photothermal response was also investigated. In this case, the excitation frequency was held constant at 100 kHz for all measurements. Optical parameters were identical to those used in the investigation of excitation frequency. A linear increase in the photothermal response with excitation voltage was expected due to the direct relationship between the resistance in the detection cell and the applied excitation voltage, based on Ohm's law. It was observed that the signal response increased linearly (correlation coefficient of 0.998) up to the maximum investigated of 9 V while the noise remained relatively independent of excitation voltage. This indicates that higher excitation voltages should be used to maximize S/N (Table 1); however, there are practical limits to the maximum applied voltage, as higher potentials cause premature degradation of the electrode material.

Computational simulations indicated an increase in signal intensity with smaller electrode spacing (Figure 3B). This was experimentally investigated using three different microchips run under identical conditions as the excitation frequency and voltage studies with electrodes spaced 25, 50, and 100 μm apart. The data obtained for DABSYL-Glu as a function of electrode spacing are shown in Table 2. The highest S/N was obtained with the 50-μm spaced electrodes for all laser powers tested. While the front height at each laser power was largest with the 25-μm spaced electrodes, the noise associated with each measurement taken using the narrowest electrode spacing was greater than that seen with the larger spacings (i.e., 50 and 100 μm) resulting in a decrease in the S/N compared to the 50-μm spacing. The source of the increased noise observed with the narrowest electrode spacing is believed to be from electrode heating by the laser. Variations in the background signal will be proportional to laser power variations (source noise) and will be more prevalent when using smaller detection spacings arising from increased light hitting the electrodes.

Optical Characterization

It has been established in studies performed on a capillary photothermal system that a linear increase in signal response is expected with higher laser powers. Traces of the raw data obtained from such an experiment performed on a microchip with electrodes spaced 50 μm apart are shown in Figure 5. For this example, the laser power was 48 mW (modulated at 20 Hz) at the detection point and the excitation was a 1-V_{p-p}, 100-kHz signal. The two traces represent data obtained from the two lock-in amplifiers. The red trace shows the conductivity signal obtained with the first lock-in amplifier (SR 810, Stanford Research Systems, Sunnyvale, CA) with an inset image showing the modulation, while the blue trace shows the photothermal response obtained with the second lock-in amplifier (SR 810, Stanford Research Systems, Sunnyvale, CA). For the laser power study the modulation frequency was held constant at 20 Hz. Electronic excitation was obtained using a 5-V_{p-p}, 100-kHz sinusoidal signal on a microchip with a 30-μm deep channel and electrodes spaced 50 μm apart. Detailed results of the laser power study are shown in Table 2. The front height and S/N were linear with respect to laser power (R^2 = 0.998). The background conductivity noise level remained fairly constant at each of the laser powers tested, with the exception of the narrowest electrode spacing investigated. This indicates that higher laser powers will give increased S/N until practical limitations such as microchip fracture or material melting occurs, or when electrical crosstalk dominates the signal.

The effect of optical modulation (chopping) frequency was also investigated. For this study a laser power of 48 mW with a 5-V_{p-p}, 100-kHz excitation signal was used on a microchip with similar dimensions to that used for the excitation frequency and voltage studies. It has been previously shown that an increase in the modulation frequency causes a decrease in the signal response.[10] It is thought that the depth of modulation increases at lower modulation frequencies, giving a higher signal response, until the point at which the wobble associated with the optical chopper dominates the noise. As shown in Figure 6 the S/N begins to roll off around 20–25 Hz for the microchip system.

Concentration Study

Using 7-second long gated injections, the response of the detection system was explored using DABSYL-Glu at concentrations in the range of 0.5–20 μM. Long injections were used to give flat topped "peaks" in order to accurately characterize the sensitivity of the detection method. This ensures that the concentration of species at the detection point is known and free from any dilution stemming from axial dispersion in the electrophoretic separations process. A logarithmic plot of the photothermal response as a function of analyte concentration is shown in Figure 7. This experiment was conducted using a laser power of 158 mW (modulated at 20 Hz) at the detection point and a 5-$V_{p\text{-}p}$, 100-kHz excitation signal on a microchip with a 30-μm deep channel and electrodes spaced 50 μm apart. Based on the detector response, an R^2 value of 0.99 is obtained, indicating a linear response with analyte concentration. Using a linear regression fit, the extrapolated limit of detection for DABSYL-Glu was calculated to be 5×10^{-9} M at a S/N of 3 under these experimental conditions. This concentration limit of detection is equivalent to an absorbance value of 4.4×10^{-7} AU using a molar absorptivity of 29,600 M^{-1} cm^{-1} for DABSYL-Glu and 30-μm pathlength. In comparison, other microchip based measurements found in the literature have calculated absorbances in the 10^{-2}–10^{-3} AU range at stated LODs.[41–48] Most measurements made using thermal lens techniques have reported absorbance detection limits in the 10^{-6}–10^{-7} range in organic solvents with higher detection limits in aqueous solutions.[49] Uchiyama *et al.* were able to obtain a concentration limit of detection for DABSYL-Ala in phosphate buffer based on a linear regression fit of 4.6×10^{-8} M at a S/N of 2 using thermal lens microscopy for detection with a capillary/microchip hybrid system.[50]

Separations

Electrophoretic separation of three DABSYL tagged amino acids (glycine, tryptophan, and proline) in 20-mM MES/20-mM His in acetonitrile/water (65:35 v/v) was performed using a photothermal detection microchip to demonstrate the feasibility of the detection method directly on a separation chip (Figure 8). Detection parameters used in this separation included a channel depth of 30 μm, detection electrodes spaced 100 μm apart, 5-$V_{p\text{-}p}$ 100-kHz excitation signal, and laser power of 48 mW modulated at 20 Hz. A 1-second gated injection was used to inject the 50-μM sample mixture. The experimentally determined S/N values for glycine, proline, and tryptophan were 480, 560, and 556, respectively. Based on these experimentally determined S/N values, 300-nM DABSYL-glycine would need to be injected onto the microchip to obtain a S/N value of 3. The analyte concentration at the detector would be less than this value due to dilution resulting from axial dispersion in the separation channel. However, this separation was not run under optimal detection conditions, namely laser power and electrode spacing. Under optimal conditions (laser power of 150 mW and electrode spacing of 50 μm), a S/N of 3 would be expected from injection of a 100-nM DABSYL-glycine sample (a 3-fold lower detection limit, based on the measured effects of laser power and electrode spacing on detection S/N ratios, described previously in this work).

Using an argon ion laser at 200 mW as a pump laser and a 15-mW He-Ne laser as a probe laser, Uchiyama *et al*. were able to detect 600-nM DABSYL-glycine in phosphate buffer with an equivalent absorbance of ~6.0×10^{-5} AU.[50] Under the given experimental conditions, both techniques demonstrate similar sensitivity levels and detection limits for DABSYL tagged amino acids. Applicability of thermal lens techniques may be more suitable when organic solutions make up the sample matrix. However, the current technique should be more advantageous in situations where separations are performed in aqueous or mixed solutions (separation of peptides and proteins, for example) because of the larger change in viscosity as a function of temperature (and thus conductivity) in comparison to refractive index.

Summary

An optical detection technique appropriate for the small volumes encountered with microfluidic devices has been developed. The detection method is based on known thermooptical principles but unlike previous methods, the current technique is based on changes in solution viscosity. The viscosity change per degree of temperature change is 50–200 times greater than that of refractive index, making this technique potentially more sensitive than other previously developed thermooptical techniques. As discussed previously, Uchiyama *et al*. showed similar sensitivities for DABSYL tagged amino acids, however each technique has its own merits and applicability.[50] For example, thermal lens microscopy may be advantageous for separations in organic based matrices, while photothermal spectroscopy will be more advantageous for separations in aqueous based solutions, including native peptide and protein separations. Proof of principle for the technique described here was previously demonstrated using a capillary-based system. The current microfluidic-based device has shown superior performance to the capillary-based system, with a limit of detection in the nM range for DABSYL-Glu corresponding to an absorbance detection limit of 0.4 μAU. In addition to having superior sensitivity to the previous capillary-based detection system, the wide range applicability of the technique also makes it a promising alternative to other detection methods commonly used with microfluidic devices. Ongoing work with the current technique includes the incorporation of ultraviolet wavelengths to make the method more amenable for the detection of an even larger number of analytes, including native proteins and peptides.

Acknowledgments

The authors thank Kevin Braun and Rose Ramsey for many insightful discussions. Funding for this project was provided by the National Institute of General Medical Sciences (Grant No. R01 GM067905-01A1) whom we thank for their continued support of this work.

References

1. Dasgupta PK, Bellamy HS, Liu H. Talanta 1993;40:341–345. [PubMed: 18965635]
2. Kahle V. Biomed Chromatogr 1999;13:93–94. [PubMed: 10191954]
3. Xue Y, Yeung ES. Anal Chem 1994;6:3575–3580.
4. Petersen NJ, Mogensen KB, Kutter JP. Electrophoresis 2002;23:3528–3536. [PubMed: 12412121]
5. Hiki S, Mawatari K, Hibara A, Tokeshi M, Kitamori T. Anal Chem 2006;78:2859. [PubMed: 16615803]
6. Weast, RC., editor. CRC Handbook of Chemistry and Physics. 51. CRC Press; Boca Raton, FL: 1970.
7. Huang X, Pang T, Gordon M, Zare R. Anal Chem 1987;59:2747–2749.
8. Huang X, Gordon MJ, Zare RN. J Chromatogr 1988;425:385–390. [PubMed: 3372649]
9. Huang X, Gordon MJ, Zare RN. J Chromatogr 1989;480:285–288.
10. Huang X, Luckey JA, Gordon MJ, Zare RN. Anal Chem 1989;61:766–770.
11. da Silva JAF, do Lago CL. Anal Chem 1998;70:4339–4343.
12. Zemann AJ, Schnell E, Volgger D, Bonn GK. Anal Chem 1998;70:563–567.
13. Laugere F, Lubking GW, Berthold A, Bastemeijer J, Vellekoop MJ. Sensors and Actuators A 2001;92:109–114.
14. Guijt RM, Baltussen E, van der Steen G, Frank H, Billiet H, Schalkhammer T, Laugere F, Vellekoop MJ, Berthold A, Sarro L, van Dedem GWK. Electrophoresis 2001;22:2537–2541. [PubMed: 11519958]
15. Guijt RM, Baltussen E, van der Steen G, Schasfoort RBM, Schlautmann S, Billiet H, Frank H, van Dedem GWK, van den Berg A. Electrophoresis 2001;22:235–241. [PubMed: 11288890]
16. Bastemeijer J, Lubking GW, Laugere F, Vellekoop MJ. Sensors and Actuators B 2002;83:98–103.
17. Laugere F, Lubking GW, Berthold A, Bastemeijer J, Vellekoop MJ. Sensors and Actuators A 2001;92:109–114.

18. Wang J, Gang Chen G, Muck AJ. Anal Chem A Pages. 2003
19. Berthold A, Laugere F, Schellevis H, de Boer CR, Laros M, Guijt RM, Sarro RM, Vellekoop MJ. Electrophoresis 2002;23:3511–3519. [PubMed: 12412119]
20. Macka M, Hutchinson J, Zemann A, Shusheng Z, Haddad PR. Electrophoresis 2003;24:2144–2149. [PubMed: 12858387]
21. Lichtenberg J, de Rooij NF, Verpoorte E. Electrophoresis 2002;23:3769–3780. [PubMed: 12432540]
22. Tanyanyiwa J, Abad-Villar EM, Fernandez-Abedul MT, Costa-Garcia A, Hoffmann W, Guber AE, Hermann D, Gerlach A, Gottschlich N, Hauser PC. Analyst 2003;128:1019–1022.
23. Wang J, Pumera M, Collins GE, Mulchandani A. Anal Chem 2002;74:6121–6125. [PubMed: 12498212]
24. Prest JE, Baldock SJ, Fielden PR, Goddard NJ, Brown BJT. Analyst 2002;127:1413–1419. [PubMed: 12475027]
25. Masar M, Zuborova M, Kaniansky D, Stanislawski B. J Sep Sci 2003;26:647–652.
26. Liu Y, Wipf DO, Henry CS. Analyst 2001;126:1248–1251. [PubMed: 11534587]
27. Prest JE, Baldock SJ, Fielden PR, Goddard NJ, Brown BJT. J Chromatogr A 2003;990:325–334. [PubMed: 12685612]
28. Zuborova M, Demianova Z, Kaniansky D, Masar M, Stanislawski B. J Chromatogr A 2003;990:179–188. [PubMed: 12685596]
29. Evenhuis CJ, Guijt RM, Macka M, Haddad PR. Electrophoresis 2004;25:3602–3624. [PubMed: 15565711]
30. Johnston SE, Fadgen KE, Jorgenson JW. Anal Chem 2006;78:5309–5315. [PubMed: 16878864]
31. Yu M, Dovichi NJ. Anal Chem 1989;61:37–40. [PubMed: 2496623]
32. Fadgen, KE. PhD Thesis. University of North Carolina; Chapel Hill, NC: 2001.
33. Johnston, SE. PhD Thesis. University of North Carolina; Chapel Hill, NC: 2005.
34. Jacobson SC, Koutny LB, Hergenröder R, Moore AW, Ramsey JM. Anal Chem 1994;66:3472.
35. Madou, MJ. Fundamentals of Microfabrication: The Science of Miniaturization. 2. CRC Press; New York, NY: 2002. p. 18-19.
36. CoventorWare ANALYZER Microfluidics Reference. Coventor, Inc; Cary, NC: 2006.
37. Tuma P, Opekar F, Stulik K. Electrophoresis 2002;23:3718–3724. [PubMed: 12432534]
38. Zemann AJ. Electrophoresis 2003;24:2125–2137. [PubMed: 12858385]
39. Kuban P, Hauser PC. Electrophoresis 2004;25:3398–3405. [PubMed: 15490445]
40. Kuban P, Hauser PC. Electrophoresis 2004;25:3387–3397. [PubMed: 15490444]
41. Jindal R, Cramer SM. J Chromatogr A 2004;1044:277–285. [PubMed: 15354449]
42. Park JS, Park KB, Shin KS, Park HD, Kim MC, Kim JR, Park SJ, Song YH. Sens Actuators B 2006;117:516–522.
43. Duggan MP, McCreedy T, Aylott JW. Analyst 2003;128:1336–1340. [PubMed: 14700226]
44. Mogensen KB, Petersen NJ, Hubner J, Kutter JP. Electrophoresis 2001;22:3930–3938. [PubMed: 11700723]
45. Kee JS, Poenar DP, Neuzil P, Yobas L. Sensors and Actuators B 2008;34:532–538.
46. Splawn BG, Lytle FE. Anal Bioanal Chem 2002;373:519–525. [PubMed: 12185563]
47. Liang Z, Chiem N, Ocvirk G, Tang T, Fluri K, Harrison DJ. Anal Chem 1996;68:1040–1046.
48. Mogensen KB, Eriksson F, Gustafsson O, Hikolarjsen RPH, Kutter JP. Electrophoresis 2004;25:3788–3795. [PubMed: 15565688]
49. Smirnova A, Proskurnin MA, Bendrysheva SN, Nedosekin DA, Hibara A, Kitamori T. Electrophoresis 2008;29:2741–2753. [PubMed: 18546176]
50. Uchiyama K, Hibara A, Sato K, Hisamoto H, Tokeshi M, Kitamori T. Electrophoresis 2003;24:179–184. [PubMed: 12652589]

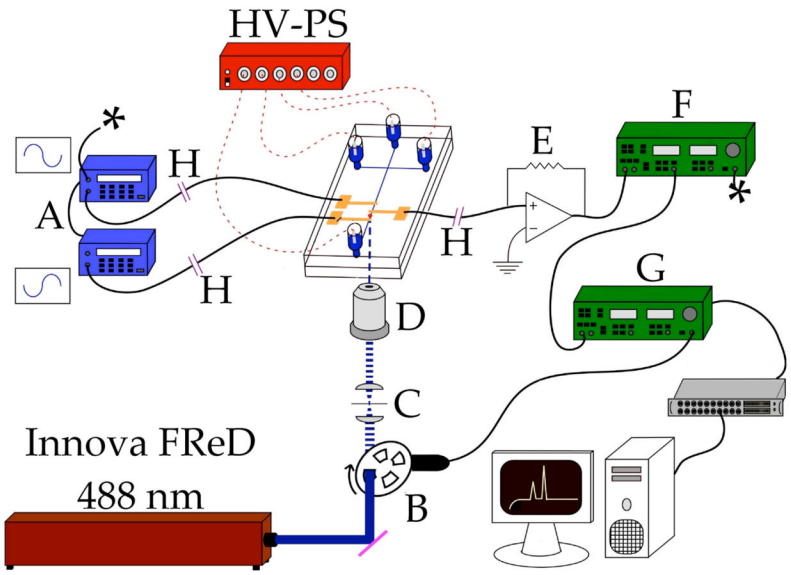

Figure 1.

Schematic of the microchip photothermal setup including optical and electrical components. The microchip with electrodes is shown in the center. Components: (HV-PS) high voltage power supply, (A) two function generators, (B) optical chopper, (C) spatial filter, (D) microscope objective, (E) feedback resistor, (F) conductivity lock-in amplifier, and (G) photothermal lock-in amplifier. The reference for the conductivity lock-in amplifier is supplied by one function generator (*) and the reference for the photothermal lock-in amplifier is supplied by the optical chopper. High voltage capacitors (H) prevent DC voltage from reaching the detection electronics.

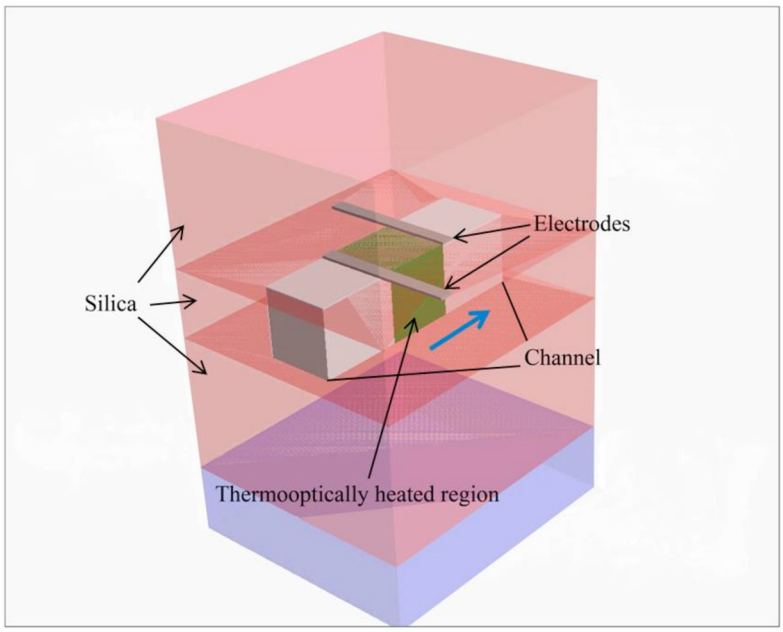

Figure 2.
Representative schematic used for CoventorWare simulations showing the thermooptically heated region where light impinges the sample, excitation and detection electrodes, channel, and fused silica substrates. The channel shown is 50 μm deep (shown for clarity); however, simulations were performed on a model with a 10-μm deep channel. Only one side of the system (i.e., only 2 of 3 electrodes) is shown. The blue arrow denotes the direction of fluid flow.

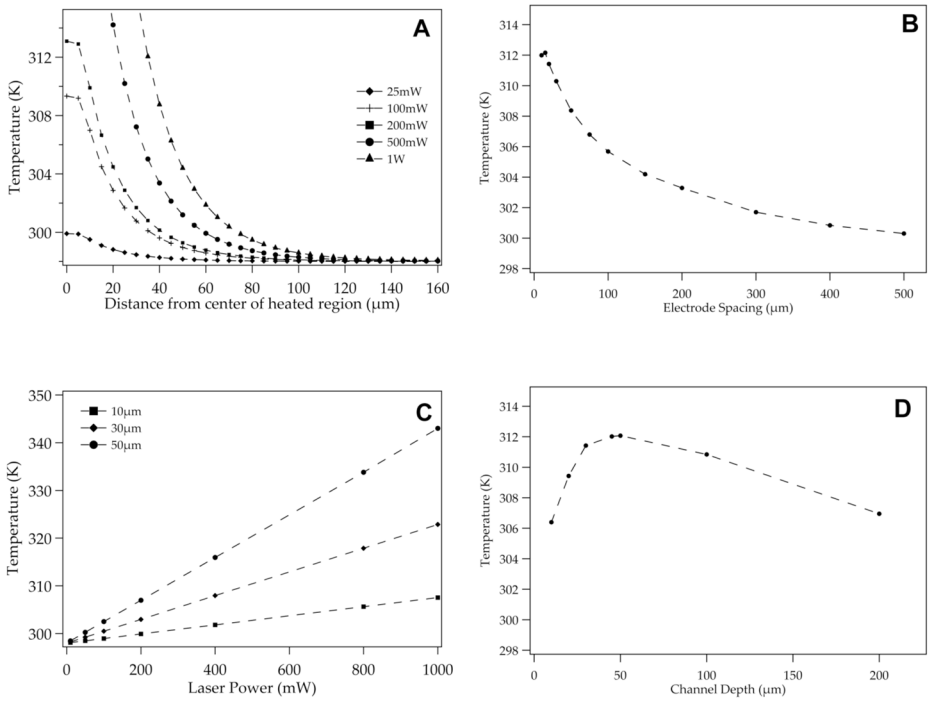

Figure 3.

Simulations showing: (A) spatial distribution of heat in a 10-μm diameter channel, (B) average temperature in the detection region as a function of electrode spacing, (C) average temperature in the region between 50 μm spaced electrodes for 10-, 30-, and 50-μm deep channels as a function of laser power, and (D) average temperature in the detection region as a function of channel depth, maintaining a channel aspect ratio of 0.25.

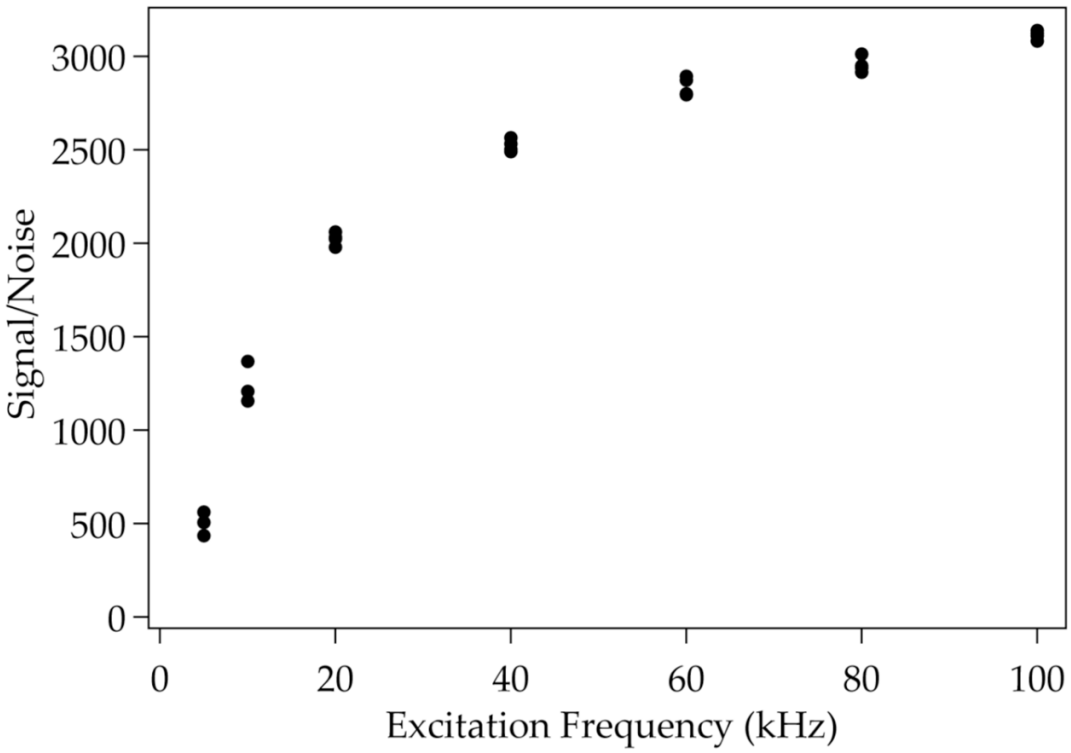

Figure 4.
Experimental data showing S/N of the photothermal response to 50-μM DABSYL-Glu as a function of excitation frequency. Conditions: 30-μm diameter channel, 50-μm electrode spacing, 5-$V_{p\text{-}p}$ excitation voltage and 48-mW laser power, modulated at 20 Hz; n=3.

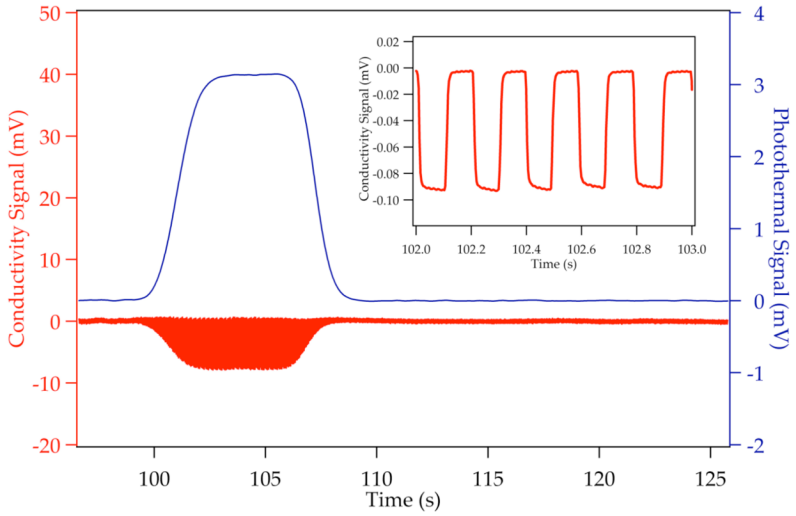

Figure 5.

Photothermal and conductivity responses obtained using a 7-second injection of 50-μM DABSYL-Glu. The inset figure shows a magnified view of the conductivity trace. The excitation for this experiment was a 1-$V_{p\text{-}p}$, 100-kHz sinusoidal signal. Laser power: 48-mW, modulated at 20 Hz. This response was obtained using a 30-μm deep channel using electrodes spaced 50 μm apart. The absolute photothermal response is ~ 3 mV, giving a S/N of ~ 1200.

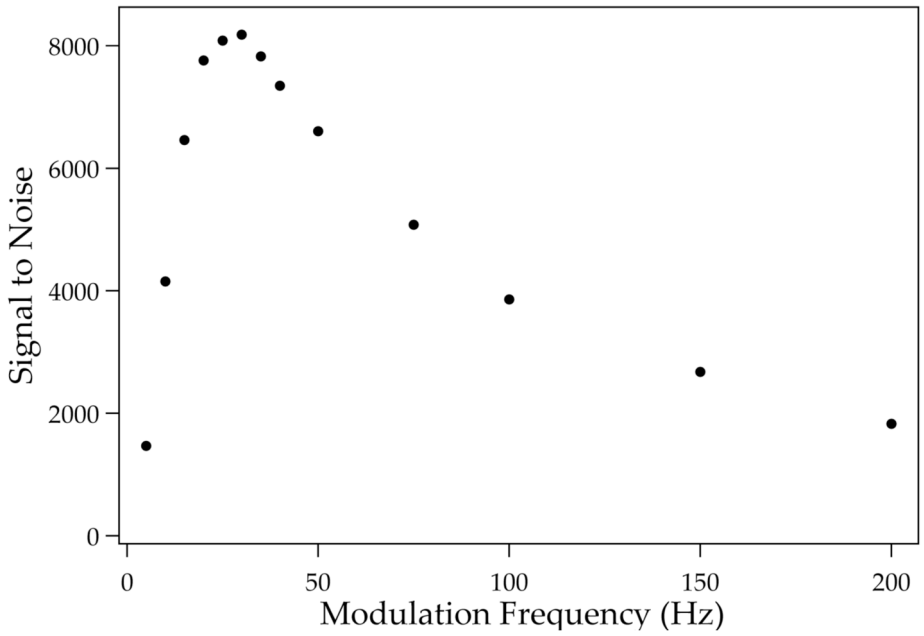

Figure 6.
Plot showing the S/N of 50 μM DABSYL-Glu as a function of modulation frequency. Conditions: 30-μm deep channel, 50-μm electrode spacing, 5-V_{p-p} excitation at 100 kHz and 48-mW laser power.

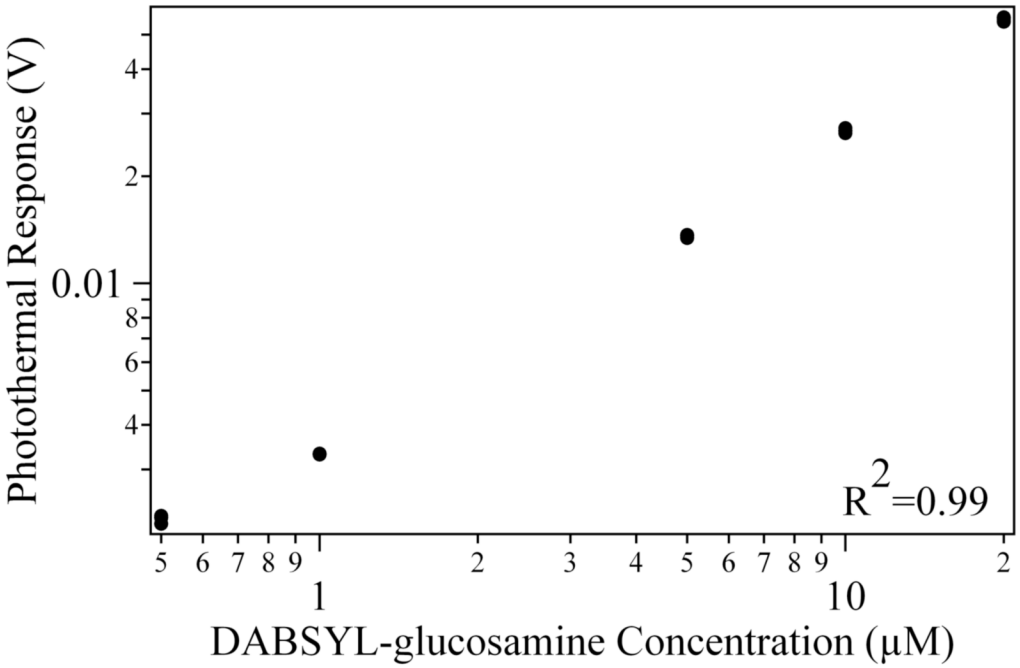

Figure 7.

Plot of the photothermal response of DABSYL-Glu as a function of concentration. Conditions: 30-μm deep channel, 50-μm electrode spacing, 5-V_{p-p} excitation voltage, 100-kHz sinusoidal signal, and 158-mW laser power modulated at 20 Hz; n=4.

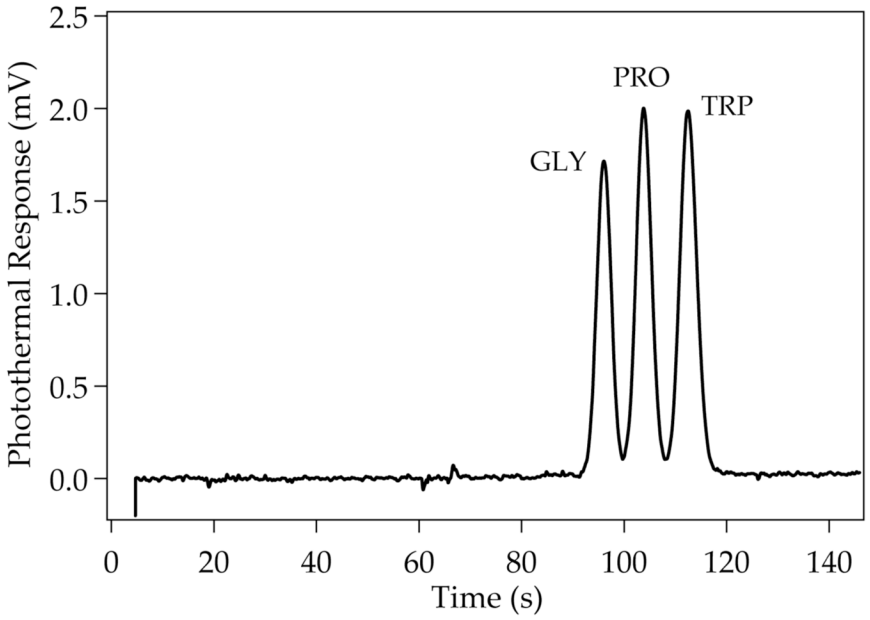

Figure 8.

Electrophoretic separation with photothermal detection of a 1-second injection of 50-μM DABSYL tagged amino acids glycine, tryptophan, and proline. The excitation was a 5-Vp-p, 100-kHz sinusoidal signal and was detected using a microchip with a 30-μm deep channel and electrodes spaced 100 μm apart. The laser intensity was 48 mW, modulated at 20 Hz.

Table 1

Summary of the photothermal response to 50-μM DABSYL-Glu using various excitation voltages. All measurements were taken in a 30-μm deep channel with electrodes spaced 50 μm apart. Application of a 5-V_{p-p} sinusoidal signal at 100 kHz and 48-mW laser power modulated at 20 Hz was used for detection. Relative standard deviations (RSD) are also given for each measurement; n=3.

excitation voltage (V_{p-p})	front height (mV) (RSD,%)	baseline noise (μV) (RSD,%)	S/N (RSD,%)
0.5	1.6 (±3.3)	2.5 (±2.7)	640 (±0.71)
1	3.1 (±1.1)	3.1 (±1.8)	1000 (±0.77)
3	10.5 (±0.35)	3.7 (±3.7)	2838 (±3.3)
5	14.6 (±0.68)	3.8 (±1.5)	3842 (±1.5)
7	21.7 (±3.2)	4.8 (±2.0)	4521 (±1.2)
9	27.5 (±0.96)	5.3 (±3.5)	5189 (±2.5)

Table 2

Summary of S/N results for 50-μM DABSYL-Glu using a microchip with 30-μm deep channels and various electrode spacings. The laser power used was modulated at 20 Hz and is stated based on the power at the detection point. Excitation was with a 5-V_{p-p}, 100-kHz sinusoidal signal. Relative standard deviations (RSD) are also given for each measurement; n=3.

Laser Power (mW)	25 μm spacing S/N (RSD,%) front height (mV) (RSD,%)	50 μm spacing S/N (RSD,%) front height (mV) (RSD,%)	100 μm spacing S/N (RSD,%) front height (mV) (RSD,%)
3.5	470 (±1.3)	1100 (±2.4)	1000 (±3.4)
	4.8 (±1.3)	2.0 (±2.4)	1.4 (±0.9)
9	370 (±1.4)	2200 (±2.1)	2000 (±4.1)
	12.5 (±2.5)	5.8 (±2.1)	3.3 (±1.5)
17	310 (±1.1)	3800 (±1.5)	2900 (±3.6)
	22.8 (±1.1)	11.4 (±1.5)	6.3 (±0.6)
28	250 (±3.9)	5600 (±1.2)	4000 (±4.4)
	37.7 (±1.4)	19.6 (±1.2)	10.5 (±0.4)
42	230 (±3.0)	7700 (±1.1)	5100 (±3.2)
	57.4 (±3.0)	31.2 (±1.1)	14.6 (±1.8)
59	230 (±2.3)	10000 (±0.6)	6700 (±2.6)
	77.2 (±2.3)	44.5 (±0.6)	20.8 (±0.4)
78	240 (±4.6)	13000 (±0.4)	7800 (±2.5)
	97.8 (±4.6)	60.8 (±0.4)	28.8 (±1.3)